

Carrier Localization and Spontaneous Formation of Two-Dimensional Polarization Domain in Halide Perovskites

Andrew Grieder,¹ Marcos Calegari Andrade,^{2,3} Hiroyuki Takenaka,²

Tadashi Ogitsu,³ Liang Z. Tan,^{4,*} and Yuan Ping^{1,5,6,†}

¹*Department of Materials Science and Engineering,*

University of Wisconsin-Madison, Madison WI 53718, USA

²*Department of Chemistry, University of California, Santa Cruz CA 95064, USA*

³*Quantum Simulations Group, Lawrence Livermore National Laboratory, Livermore CA 94551, USA*

⁴*Molecular Foundry, Lawrence Berkeley National Lab, Berkeley CA 94720, USA*

⁵*Department of Physics, University of Wisconsin, Madison, WI, 53706, USA*

⁶*Department of Chemistry, University of Wisconsin, Madison, WI, 53706, USA*

(Dated: February 28, 2025)

Halide perovskites are known for their rich phase diagram and superior performance in diverse optoelectronics applications. The latter property is often attributed to the long electron-hole recombination time, whose underlying physical mechanism has been a long-standing controversy.

In this work, we investigate the transport and localization properties of electron and hole carriers in a prototypical halide perovskite (CsPbBr_3), through *ab initio* tight-binding non-adiabatic dynamics approach for large-scale (tens of nm size) supercell calculations. We found distinct structural, lattice polarization, and electron-phonon coupling properties at low (below 100 K) and high temperatures, consistent with experimental observations. In particular, at low temperature we find spontaneous formation of polar grain-boundaries in the nonpolar bulk systems, which result in two-dimensional polarization patterns that serve to localize and separate electrons and holes. We reveal phonon-assisted variable-range hopping mostly responsible for low-temperature transport, and their characteristic frequency correlates with temperature-dependent phonon power spectrum and energy oscillation frequency in nonadiabatic dynamics. We answer the critical questions of long electron-hole recombination lifetime and offer the correlation among polarization domains, electron-phonon couplings, and photocarrier dynamics.

Lead halide perovskites (LHPs) have received significant attention in the past decade's due to their remarkable optoelectronic properties, including low carrier recombination rates, high carrier mobility, and long carrier diffusion lengths [1–4]. The unique combination of properties has resulted in LHPs superior applications in solar cells, light-emitting diodes, and other electronic devices [5–7]. Despite extensive research, the underlying mechanisms that facilitate outstanding electronic properties such as long electron-hole recombination time remain under debate and thus demand clarification in order to widely apply LHPs in accessible technologies [8–10].

Proposed mechanisms to explain long electron-hole recombination lifetimes and diffusion lengths in LHPs include, charge carrier localization through formation of large polarons or ferroelectric domains. Large polarons form due to strong electron-phonon couplings and result in localization of excess holes or electrons coupled to lattice distortions over multiple unit cells [11–17]. However, it remains a subject of debate whether large polarons provide a complete explanation of carrier dynamics in LHPs [9, 18, 19]. Alternatively, the formation of ferroelectric domains cause polar regions which force electron and hole trajectories to be physically separated, thus avoid recombination [20, 21]. However, the presence or absence of ferroelectricity in LHPs has been a long-standing controversy.

In this work, carrier dynamics and localization are in-

vestigated in a prototypical LHP, CsPbBr_3 . A main challenge to accurately simulate carrier dynamics is the requirement to include a quantum mechanical description of electrons/holes, supercells with length scale on the order of tens of nanometers, and time propagation long enough to capture relevant dynamics. These requirements make direct quantum mechanical calculations such as density functional theory (DFT) intractable. To overcome the computational challenge, we adopt a combined technique utilizing time-dependent first-principles tight-binding (FPTB) description for electrons/holes and machine learning inter-atomic potentials for ion-ion interactions, under an Ehrenfest dynamics framework (including additional electronic forces from FPTB).

The FPTB model is constructed using physically motivated descriptors to efficiently and accurately compute the Hamiltonian given instantaneous ionic positions [22]. Once parameterized, the FPTB model faithfully reproduces DFT electronic structures including effects from thermal fluctuations. The atomic positions are determined by machine learning (ML) inter-atomic potentials which allow for accurate descriptions of the octahedral tilting, not captured by standard pairwise potentials. Accurate potential development [23–25], including the use of ML [26], has been key to the study of halide perovskite dynamics. The tilting patterns are benchmarked against DFT and provide significant improvement over pairwise potentials, see SI Section VI for details and compari-

son [25]. Lastly, the charge carrier forces are computed from the instantaneous FPTB Hamiltonian in combination with the ML-forces to propagate the ions in time using LAMMPS [27]. Validation of all the components of the model can be found in the SI Sections II and VI. The combined approach allows for FPTB nonadiabatic dynamics with supercells on the order of tens of nanometers and sufficient statistical sampling to compute key observables such as carrier diffusion coefficients, mobility, and local lattice polarization, then compare with past experimental and theoretical work [4, 28, 29].

A key finding of this study is the natural formation of nano-domains at low temperature. During simulated annealing, polar 90° twinning grain-boundaries spontaneously form within the nonpolar bulk material. Such twinning grain-boundaries have also been observed in single crystal experiments of CsPbBr_3 [30, 31], which show the accuracy of our theoretical method to predict inhomogeneous complex structure formation. The grain-boundaries are found to induce planes of local lattice polarization along the grain-boundaries on the order of $20 \mu\text{C}/\text{cm}^2$. The nature of the polarization patterns serves as a novel mechanism of electron-hole localization and separation, in addition to formation of ferroelectricity and large polarons.

Other kinds of grain-boundaries have also been proposed to increase recombination times [32], although they involve tilting of entire crystalline domains and would not arise spontaneously, unlike the kind considered here. At high temperatures, the local polarization becomes dominated by thermal fluctuations, and carrier transport transitions from a hopping mechanism of localized carriers to band transport. The transition temperature between the two mechanisms is predicted by our mobility simulations and agrees well with experiments [29].

Carrier mobility and temperature dependence– Electron mobility in CsPbBr_3 without nano-domains is computed for a range of temperatures to examine the electron-phonon coupling effects on transport properties. Diffusion coefficients (D) are determined from the spread of a Gaussian wave-packet in a $20 \times 20 \times 20$ supercell. Carrier mobility (μ) is then computed from diffusion coefficients using the Einstein relation ($\mu = eD(k_B T)^{-1}$) and reported in Fig. 1a), see SI Section III for details. The $20 \times 20 \times 20$ supercell was found to be sufficiently converged with respect to supercell sizes, see SI Fig. S5

The computed mobility in the high-temperature regime $T > 100$ K, has a power law $T^{-1.41}$ consistent with experiment [4, 29]. To understand which phonon modes contribute to the high temperature mobility power law, the phonon mode projections and phonon power-spectrum for temperatures of 20, 100, and 200 K were analyzed (Fig. 1c). The phonon modes associated with Br motion are expected to have the greatest impact on mobility as these modes are related to octahedral rocking

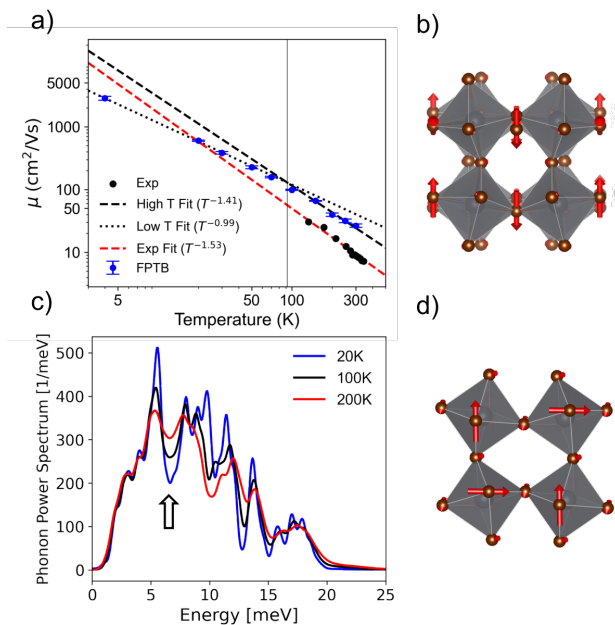


FIG. 1. Computed temperature-dependent carrier mobility including important phonon contributions without nano-domains. a) Electron mobility at increasing temperature fit to low temperature (below 100 K) and high temperature range (above 100 K). Experiments (Exp) are from Ref [4]. b) and d) Phonon modes whose occupations significantly increase with temperature at 7 meV, indicated in panel c). c) Phonon power spectrum of Br ions at 20, 100, and 200K.

modes. The Br projected phonon power spectrum shows a significant increase in occupation around 7 meV with increasing temperature, and a decrease in phonon occupation around 10 meV (Fig. 1c). The modes responsible for the increase around 7 meV are the optical rocking modes, depicted in Fig. 1b and Fig. 1d. The rocking octahedra cause the Pb-Br bond distances to fluctuate, impeding carrier mobility. The mobility was found to have different temperature power laws below and above ~ 100 K, Fig. 1a, consistent with experiments[29]. Experimentally, the temperature dependence (T^β) of the mobility transitions at ~ 80 K from $\beta > 0$ below 80 K to $\beta \approx -1.5$ above 80 K. The positive temperature dependence power law below 80 K indicates thermally-activated transport of localized carriers dominates at low temperature, and suggests that phonons alone cannot explain the low temperature mobility.

Annealed structure and spontaneous formation of two-dimensional domains– Low temperature carrier properties are investigated in an annealed structure generated with the following procedure using the ML-potentials. The initial structure was thermalized for 100 ps at 200 K, then quenched at 5 K/ps to 20 K and simulated for another 100 ps of MD, under the NPT ensemble. After the annealing procedure, the lattice vectors were then fixed to the average lattice vectors of the final 10 ps and al-

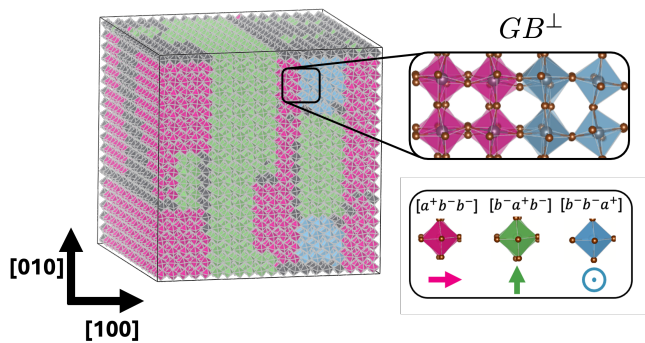


FIG. 2. Grain-boundary formed during simulated annealing. Legends indicate grain-boundary classification and color coding for in-phase tilting axis, referred to as *ip*-axis in the text.

lowed to equilibrate under the NVT ensemble for 100 ps. Finally, non-adiabatic Ehrenfest dynamics is simulated with the time dependent FPTB Hamiltonian and ML potentials for another 1.4 ps, to compute local lattice polarization, investigate carrier localization and transport properties. The final structure is presented in Fig. 2.

The spontaneous formation of nano-domains occurs during the annealing simulation. The nano-domains have twinning grain-boundaries with 90° rotations, consistent with experiments on single crystal CsPbBr₃ [30, 31]. Additionally, the grain-boundaries are found to be stable, lasting for longer than 100 ps of MD.

The individual domains are nonpolar, with *Pnma* symmetry which has a Glazer notation of $(a^+b^-b^-)$ [33]. This structure has a single axis (a^+) along which there is in-phase octahedral tilting and two axes (b^-) with out-of-phase tilting. The unique in-phase tilting axis will be referred to as the *ip*-axis in the subsequent text. Excluding tilting of entire crystalline domains, there exist 3 possible orientations for the nano-domains, with *ip*-axis oriented along [100], [010], and [001], depicted in Fig. 2.

Nano-domains of all three orientations are present in the annealed structure. The dominant tilting patterns have the *ip*-axis in the [100] (pink) and [010] (green) direction, with one smaller domain with the *ip*-axis in the [001] (blue) direction. In Fig. 2, the domains can be seen to extend the entire (100) plane. This indicates the twinning grain-boundaries prefer to form in parallel, which is consistent with experimental observation [30, 31]. These 90° twinning grain-boundaries can be categorized into two types. The first type, denoted as GB^\perp , has one domain with the *ip*-axis normal to the grain-boundary and in the other domain the *ip*-axis is parallel to the grain-boundary (Fig. 2). In the second type, denoted as GB^\parallel , the *ip*-axis of both domains are parallel to the grain-boundary (SI Fig. S9c). The grain-boundaries observed

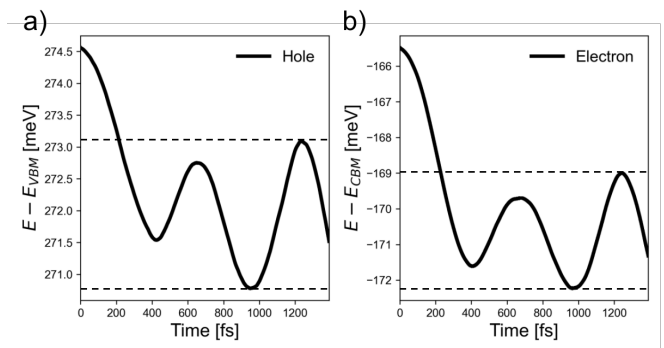


FIG. 3. Change in energy from pristine eigenstate during Ehrenfest dynamics in the nano-domain structure. a) Holes with energy referenced to VBM and b) electrons with energy referenced to CBM of the pristine crystalline system.

here are almost entirely of the GB^\perp type suggesting the twinning boundaries have lower energy when the *ip*-axis is rotated perpendicularly rather than twisted.

Carrier localization and variable range hopping— To investigate the effects of the domain structure on carrier dynamics, we simulate FPTB Ehrenfest dynamics with one extra electron or hole in the supercells with nano-domains. The initial wave function is set to the eigenstates of pristine CsPbBr₃ structure, using the VBM for holes and CBM for electrons. The initial condition ensures homogeneous distributions of the wave function, avoiding any bias in wave function localization. Note that this is in contrast to the initial state used in the mobility calculations where the wave function was initialized as a Gaussian wave-packet. Since once the Gaussian wave-packet reaches the periodic boundary, it interferes with itself before localization occurs, and was not used to investigate localization.

The initial charge density consisted of an extended distribution of electron and hole carriers becomes localized during the simulation. The hole and electron localize at spatially separated locations because of the local polarization as discussed below. The electron localizes in a pancake shape which can be seen by the Gaussian fitting in SI Fig. S12, where the charge density is extended in the YZ-plane and narrow in the X direction. Both electrons and holes become localized after around 400 fs as seen in SI Fig. S11a. After localization, the energy oscillates around 170 meV below the CBM for electrons and 270 meV above the VBM for holes, Fig. 3. The oscillations in energy arise from interaction with phonons, indicating phonon-assisted electron hopping between localized sites. The phonon induced oscillations are confirmed in SI Fig. S10 where the energy is constant in the absence of ionic motion.

Additionally, the energy oscillation frequency for both the electron and hole in Fig. 3 (around 1.7 THz) coincide with the critical optical phonon mode around 7

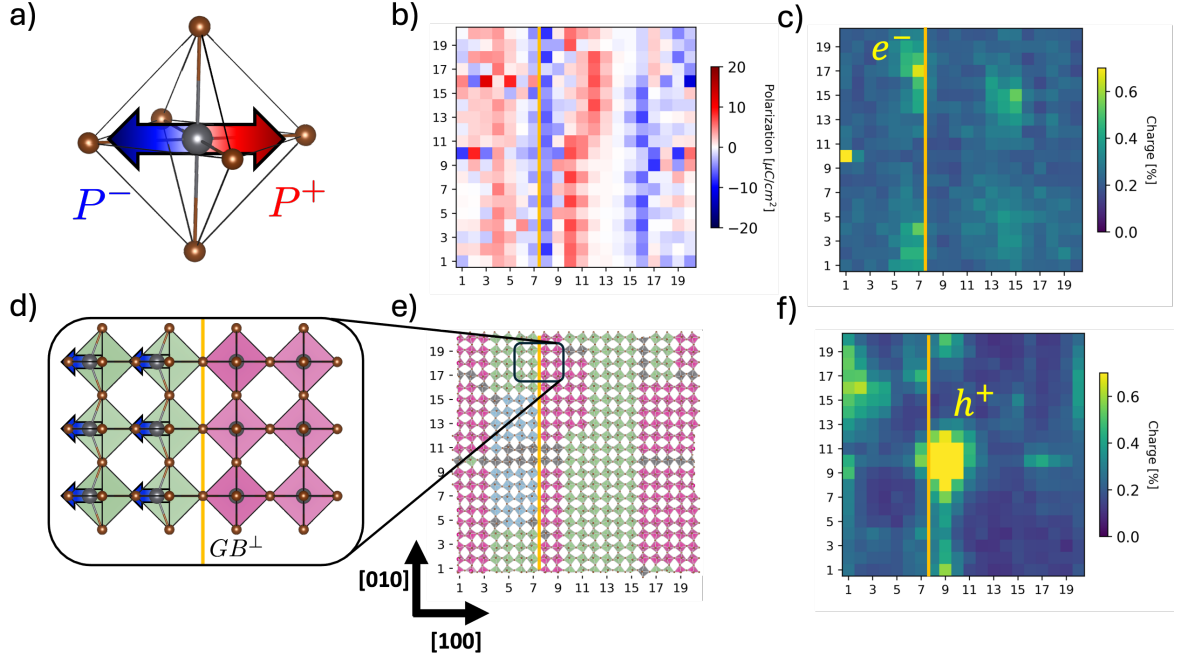


FIG. 4. Relation among domain boundaries, local polarization, and electron/hole localization. a) Schematic depiction of local polarization (P) of $PbBr_6$ octahedra. b) Local polarization in the $[100]$ direction averaged along the (001) plane. Polarization in units of $\mu C/cm^2$. 2D projection of carrier density onto the (001) plane for electrons c) and holes f). The boundary between layer 7 and 8 is marked with an orange line in panels b), c), e), f). d) is schematic on how GB^\perp induces dipole moment in layer with ip -axis parallel to the grain-boundary. e) Structure from simulated annealing with octahedra colored based on tilting pattern.

meV in Fig. 1c, which further supports the mechanism of phonon-assisted electron hopping. The low temperature transport can be explained by the Mott's variable range hopping (VRH) given in Eq. 1 [34]. Its conductivity σ 's power law is $T^{-1/4}$, matching well with the experimental temperature dependent mobility below 100 K [29]:

$$\sigma = \sigma_0 \exp\left(-\left(\frac{T_M}{T}\right)^{\frac{1}{4}}\right) \quad (1)$$

$$\sigma_0 = 3e^2\nu_{ph}\left(\frac{g_0\xi}{8\pi k_B T}\right)^{\frac{1}{2}} \quad (2)$$

$$T_M = \frac{\beta}{k_b g_0 \xi^3}. \quad (3)$$

Here e is the electron charge, k_b is the Boltzmann constant, ν_{ph} is characteristic phonon frequency, T is the temperature, ξ is the localization length, and g_0 is the density of states at the CBM such that the electron density at 10K is $2.0 \times 10^{15} cm^{-3}$. The numerical constant β is related to the critical percolation concentration, where we use $\beta = 21.2$ provided in Ref [35]. The localization length is estimated to be $\xi = 1.2 \pm 0.1 nm$. It is computed

from the full width half maximum of a Gaussian fitting of the electron charge density in the $[100]$ direction averaged over the trajectory, with an example snapshot in Fig. S12. The characteristic phonon frequency is extracted from the energy oscillations to be $\nu_{ph} = 1.7 THz$. By using $\mu = \sigma/en$ with a carrier density of $2.0 \times 10^{15} cm^{-3}$, we obtain electron carrier mobility $\sim 4 cm^2/Vs$. This is consistent with the experimental mobility measurements [29] in dark in terms of order of magnitude and temperature power-law.

Local Polarization and Electron-Hole Separation – Finally, the local polarization of the $PbBr_6$ octahedra is computed to identify the effects of structural polarization on electron/hole localization (Fig. 4). The local polarization is computed as $P = qd/V$ where P is the polarization, q is the Born Effective Charge of Pb, d is the displacement of the Pb ion from the center of the octahedra, and V is the volume of the octahedra. Ionic positions must be averaged over individual MD snapshots before computing local polarization in order to remove the transient local polarization caused by thermal fluctuations. The net polarization was found to be minimized after around 50 MD snapshots and thus used for all local polarization calculations reported in this work. While the net polarization is close to zero after averaging (SI Fig. S8), the magnitude of local polarization remains on

the order of several tens of $\mu\text{C}/\text{cm}^2$ (Fig. 4b), consistent with previous *ab initio* local polarization in CsPbBr_3 at the ferroelectric relaxor phase [28].

The main grain boundary, GB^\perp , has no inversion or roto-inversion symmetry, thus allowing polarity. This manifests as Pb ions shifting away from the grain-boundary in the domain with *ip*-axis parallel to the boundary plane, penetrating about 3-4 layers deep, while the Pb ions in the other domain have minimal shift away from the center of octahedra. The overall dipole moment of GB^\perp points normal to the grain boundary and is located in the domain with the *ip*-axis parallel to the boundary. This is illustrated in Fig. 4d, and confirmed in the constructed grain-boundaries, SI Fig. S9b. The polarized domain always has the *ip*-axis parallel to the grain boundary, indicating the PbBr_6 octahedra are more easily polarized along the out-of-phase direction.

The lattice polarization induced by the grain-boundaries explains the nature of carrier localization. Being polar, GB^\perp drives electrons to one side of the grain-boundary, while driving holes to the opposite side. This is supported by Fig. 4c and f, which shows electrons driven in the direction of local dipole moment (i.e. in the same direction as the local displacement of Pb ions), and the holes driven in the opposite direction. These planes of local polarization formed at the grain-boundaries provides a new mechanism for electron and hole localization and separation. Due to the long lived nature of the grain-boundaries and local polarization the electrons and holes tend to remain separated, thus resulting in long electron-hole recombination lifetime.

Conclusion— From our FPTB non-adiabatic dynamics simulations, a picture of hopping transport in CsPbBr_3 emerges at low temperature where electrons and holes are localized on the opposite sides of polar grain-boundaries of nano-domains. At low temperature, twinning grain-boundaries give rise to local polarization along the boundary. Given the experimental evidence of the 90° twinning grain-boundaries in single crystals, the domain boundaries and induced local polarizations offer a new mechanism to explain long electron-hole recombination lifetime in halide perovskites below 100 K. Because of the two-dimensional nature of nano-domain grain-boundaries, these results suggest a connection to experiments detecting reduced-dimensional transport in bulk halide perovskites. The possibility of such nano-domain grain-boundaries seeding or interacting with anisotropic electron-phonon effects such as 2D polarons or soft modes [17, 19, 36] remains to be investigated in the future.

Acknowledgments We acknowledge support from the Computational Materials Sciences Program funded by the US Department of Energy, Office of Science, Basic Energy Sciences, Materials Sciences and Engineering Division for the materials application and development of *ab initio* tight-binding code. We acknowledge support from

the computational chemical science program within the Office of Science at DOE under grant No. DE-SC0023301 for the code development of tight-binding-LAMMPS interfaces and parallelization. Additional support for data analysis and interpretation was provided by user program of the Molecular Foundry, Lawrence Berkeley National Laboratory, supported by the Office of Science, Office of Basic Energy Sciences, of the U.S. Department of Energy under Contract No. DE-AC02-05CH11231.

* lztan@lbl.gov

† yping3@wisc.edu

- [1] S. D. Stranks, G. E. Eperon, G. Grancini, C. Menelaou, M. J. P. Alcocer, T. Leijtens, L. M. Herz, A. Petrozza, and H. J. Snaith, *Science* **342**, 341 (2013).
- [2] L. M. Herz, *ACS Energy Letters* **2**, 1539 (2017).
- [3] T. W. Crothers, R. L. Milot, J. B. Patel, E. S. Parrott, J. Schlipf, P. Müller-Buschbaum, M. B. Johnston, and L. M. Herz, *Nano Letters* **17**, 5782 (2017).
- [4] E. M. Hutter, M. C. Gélvez-Rueda, A. Osherov, V. Bulović, F. C. Grozema, S. D. Stranks, and T. J. Savenije, *Nature Materials* **16**, 115 (2017).
- [5] H. J. Snaith, *The Journal of Physical Chemistry Letters* **4**, 3623 (2013), publisher: American Chemical Society.
- [6] S. Kazim, M. K. Nazeeruddin, M. Grätzel, and S. Ahmad, *Angewandte Chemie International Edition* **53**, 2812 (2014).
- [7] S. D. Stranks and H. J. Snaith, *Nature Nanotechnology* **10**, 391 (2015).
- [8] D. A. Egger, A. Bera, D. Cahen, G. Hodes, T. Kirchartz, L. Kronik, R. Lovrincic, A. M. Rappe, D. R. Reichman, and O. Yaffe, *Advanced Materials* **30**, 1800691 (2018).
- [9] M. J. Schilcher, P. J. Robinson, D. J. Abramovitch, L. Z. Tan, A. M. Rappe, D. R. Reichman, and D. A. Egger, *ACS Energy Letters* **6**, 2162 (2021).
- [10] L. Martiradonna, *Nature Materials* **17**, 377 (2018).
- [11] J. M. Frost, *Phys. Rev. B* **96**, 195202 (2017), publisher: American Physical Society.
- [12] A. J. Neukirch, W. Nie, J.-C. Blancon, K. Appavoo, H. Tsai, M. Y. Sfeir, C. Katan, L. Pedesseau, J. Even, J. J. Crochet, G. Gupta, A. D. Mohite, and S. Tretiak, *Nano Letters* **16**, 3809 (2016), pMID: 27224519, <https://doi.org/10.1021/acs.nanolett.6b01218>.
- [13] X.-Y. Zhu and V. Podzorov, *The Journal of Physical Chemistry Letters* **6**, 4758 (2015), pMID: 26575427.
- [14] K. Miyata, D. Meggiolaro, M. T. Trinh, P. P. Joshi, E. Mosconi, S. C. Jones, F. D. Angelis, and X.-Y. Zhu, *Science Advances* **3**, e1701217 (2017).
- [15] C. Wolf, H. Cho, Y.-H. Kim, and T.-W. Lee, *ChemSusChem* 10.1002/cssc.201701284 (2017).
- [16] K. Miyata, T. L. Atallah, and X.-Y. Zhu, *Science Advances* **3**, e1701469 (2017).
- [17] F. Ambrosio, J. Wiktor, F. D. Angelis, and A. Pasquarello, *Energy & Environmental Science* **11**, 101 (2018), publisher: Royal Society of Chemistry.
- [18] M. Sendner, P. K. Nayak, D. A. Egger, S. Beck, C. Müller, B. Epping, W. Kowalsky, L. Kronik, H. J. Snaith, A. Pucci, and R. Lovrincić, *Mater. Horiz.* **3**, 613 (2016).

- [19] F. Wang, Y. Fu, M. E. Ziffer, Y. Dai, S. F. Maehrlein, and X.-Y. Zhu, *Journal of the American Chemical Society* **143**, 5 (2021), pMID: 33320656, <https://doi.org/10.1021/jacs.0c10943>.
- [20] J. M. Frost, K. T. Butler, F. Brivio, C. H. Hendon, M. van Schilfgaarde, and A. Walsh, *Nano Letters* **14**, 2584 (2014), pMID: 24684284, <https://doi.org/10.1021/nl500390f>.
- [21] S. Liu, F. Zheng, N. Z. Koocher, H. Takenaka, F. Wang, and A. M. Rappe, *The Journal of Physical Chemistry Letters* **6**, 693 (2015), pMID: 26262488, <https://doi.org/10.1021/jz502666j>.
- [22] D. J. Abramovitch, W. A. Saidi, and L. Z. Tan, *Physical Review Materials* **5**, 085404 (2021).
- [23] C. M. Handley and C. L. Freeman, *Phys. Chem. Chem. Phys.* **19**, 2313 (2017).
- [24] T. Hata, G. Giorgi, K. Yamashita, C. Caddeo, and A. Mattoni, *The Journal of Physical Chemistry C* **121**, 3724 (2017).
- [25] S. R. G. Balestra, J. Manuel Vicent-Luna, S. Calero, S. Tao, and J. A. Anta, *Journal of Materials Chemistry A* **8**, 11824 (2015), publisher: Royal Society of Chemistry.
- [26] R. Jinnouchi, J. Lahnsteiner, F. Karsai, G. Kresse, and M. Bokdam, *Physical Review Letters* **122**, 225701 (2019).
- [27] A. P. Thompson, H. M. Aktulga, R. Berger, D. S. Bolinteanu, W. M. Brown, P. S. Crozier, P. J. in 't Veld, A. Kohlmeyer, S. G. Moore, T. D. Nguyen, R. Shan, M. J. Stevens, J. Tranchida, C. Trott, and S. J. Plimpton, *Comp. Phys. Comm.* **271**, 108171 (2022).
- [28] Q. Qian, Z. Wan, H. Takenaka, J. K. Keum, T. J. Smart, L. Wang, P. Wang, J. Zhou, H. Ren, D. Xu, Y. Huang, Y. Ping, and X. Duan, *Nature Nanotechnology* **18**, 357 (2023), number: 4 Publisher: Nature Publishing Group.
- [29] Y. Wang, Z. Wan, Q. Qian, Y. Liu, Z. Kang, Z. Fan, P. Wang, Y. Wang, C. Li, C. Jia, Z. Lin, J. Guo, I. Shakir, M. Goorsky, X. Duan, Y. Zhang, Y. Huang, and X. Duan, *Nature Nanotechnology* **15**, 768 (2020), publisher: Nature Publishing Group.
- [30] X. Zhang, F. Wang, B.-B. Zhang, G. Zha, and W. Jie, *Crystal Growth & Design* **20**, 4585 (2020).
- [31] H. Xie, B. Jin, P. Luo, Q. Zhou, D. Yang, and X. Zhang, *ACS Applied Materials & Interfaces* **16**, 54252 (2020).
- [32] Y. Wang, W.-H. Fang, R. Long, and O. V. Prezhdo, *J. Phys. Chem. Lett.* **10**, 1617 (2019), publisher: American Chemical Society.
- [33] A. M. Glazer, *Acta Crystallographica Section B* **28**, 3384 (1972), <https://doi.org/10.1107/S0567740872007976>.
- [34] N. F. Mott, *Philosophical Magazine* **19**, 835 (1969).
- [35] B. I. Shklovskii and A. L. Efros, *Electronic properties of doped semiconductors*, Vol. 45 (Springer Science & Business Media, 2013).
- [36] T. Lanigan-Atkins, X. He, M. J. Krogstad, D. M. Pajerowski, D. L. Abernathy, G. N. M. N. Xu, Z. Xu, D.-Y. Chung, M. G. Kanatzidis, S. Rosenkranz, R. Osborn, and O. Delaire, *Nat. Mater.* **20**, 977 (2021), publisher: Nature Publishing Group.